The evolution of the corona in MAXI J1535−571 through type-C quasi-periodic oscillations with *Insight*-HXMT

Yuexin Zhang,[1,2]⋆ Mariano Méndez,[1] Federico García,[1,8] Shuang-Nan Zhang,[2,5] Konstantinos Karpouzas,[1,3] Diego Altamirano,[3] Tomaso M. Belloni,[4] Jinlu Qu,[2,5] Shu Zhang,[2] Lian Tao,[2] Liang Zhang,[3,2] Yue Huang,[2] Lingda Kong,[2,5] Ruican Ma,[2,5] Wei Yu,[2,5] Divya Rawat,[6,7] and Candela Bellavita[9]

[1]*Kapteyn Astronomical Institute, University of Groningen, P.O. BOX 800, 9700 AV Groningen, The Netherlands*
[2]*Key Laboratory of Particle Astrophysics, Institute of High Energy Physics, Chinese Academy of Sciences, Beijing 100049, People's Republic of China*
[3]*School of Physics and Astronomy, University of Southampton, Southampton, SO17 1BJ, UK*
[4]*INAF-Osservatorio Astronomico di Brera, via E. Bianchi 46, I-23807 Merate, Italy*
[5]*University of Chinese Academy of Sciences, Chinese Academy of Sciences, Beijing 100049, People's Republic of China*
[6]*Department of physics, IIT Kanpur, Kanpur, Uttar Pradesh 208016, India*
[7]*Inter-University Center for Astronomy and Astrophysics, Ganeshkhind, Pune 411007, India*
[8]*Instituto Argentino de Radioastronomía (CCT La Plata, CONICET; CICPBA; UNLP), C.C.5, (1894) Villa Elisa, Buenos Aires, Argentina*
[9]*Facultad de Ciencias Astronómicas y Geofísicas, Universidad Nacional de La Plata, Paseo del Bosque, B1900FWA La Plata, Argentina*

ABSTRACT

Type-C quasi-periodic oscillations (QPOs) in black hole X-ray transients can appear when the source is in the low-hard and hard-intermediate states. The spectral-timing evolution of the type-C QPO in MAXI J1535−571 has been recently studied with *Insight*-HXMT. Here we fit simultaneously the time-averaged energy spectrum, using a relativistic reflection model, and the fractional rms and phase-lag spectra of the type-C QPOs, using a recently developed time-dependent Comptonization model when the source was in the intermediate state. We show, for the first time, that the time-dependent Comptonization model can successfully explain the X-ray data up to 100 keV. We find that in the hard-intermediate state the frequency of the type-C QPO decreases from 2.6 Hz to 2.1 Hz, then increases to 3.3 Hz, and finally increases to ∼ 9 Hz. Simultaneously with this, the evolution of corona size and the feedback fraction (the fraction of photons up-scattered in the corona that return to the disc) indicates the change of the morphology of the corona. Comparing with contemporaneous radio observations, this evolution suggests a possible connection between the corona and the jet when the system is in the hard-intermediate state and about to transit into the soft-intermediate state.

Key words: accretion, accretion discs – stars: individual: MAXI J1535−571 – stars: black holes – X-rays: binaries

1 INTRODUCTION

Black hole low-mass X-ray binaries (LMXBs) consist of a low-mass star and a central black hole which accretes materials from the star via Roche-lobe overflow. The inner part of an accreting black hole system includes an accretion disc and a hot Comptonization region, which is called the corona (for a review, see Gilfanov 2010). As the accretion disc is close to the black hole, the infalling gas releases strong gravitational energy, producing a multi-temperature blackbody emission that can be detected with a temperature around 0.3–2.0 keV in the soft X-ray band. Some of the soft photons are inverse Comptonized into hard X-ray photons in the corona, producing roughly a power-law continuum in the energy spectrum (see Done et al. 2007, for a review). A fraction of the Comptonized photons illuminate the inner accretion disc and can be Compton back-scattered in the disc, producing a relativistic reflection spectrum with characteristic emission lines, among which the most prominent feature is a broad iron K_α

line around 6.4 keV, and a Compton hump at around 20 keV (Fabian et al. 1989; García et al. 2014). Due to the relativistic property of the spacetime, the X-ray reflection spectrum has recently been developed as a powerful tool to test General Relativity (for a review, see Bambi et al. 2021).

A typical outburst of a black hole X-ray transient follows a 'q' path in the hardness intensity diagram (HID; Homan et al. 2001; Fender et al. 2004), showing a hysteresis phenomenon between the soft and hard states (Maccarone & Coppi 2003). Before the outburst, the source spends time in quiescence with the X-ray luminosity being several orders of magnitude lower than during outburst. As the outburst starts, the source enters the low-hard state with a dominant hard-photon emission; as mass accretion rate from the disc onto the black hole increases the source at some point quickly (on the order of days) transits to the high-soft state, during which the X-ray spectrum is disc dominated and the power-law emission becomes steeper; finally the source returns back to the low-hard state and eventually to quiescence as mass accretion rate decreases; a relativistic jet can appear in the transitions between the hard and the soft states (Fender

⋆ E-mail: yzhang@astro.rug.nl

et al. 2004; Remillard & McClintock 2006). Usually two types of relativistic jets are observed in these sources; the jets can be classified by the radio spectral index and the jet morphology observed: a small-scale, optically thick, steady jet and an extended, optically thin, transient jet (for a review, see Fender 2006). In the hard state, or even the hard-intermediate state, a steady jet is observed (e.g., Fender 2001; Stirling et al. 2001; Russell et al. 2019), while during the transition from the the hard-intermediate to the soft-intermediate state, the emission of the steady jet is quenched (Fender et al. 2004; Russell et al. 2011). Around the transition to the soft state, no steady jet is observed but a transient jet is launched, which is bright and consists of discrete relativistic ejecta from the black hole (Mirabel & Rodríguez 1994; Tingay et al. 1995; Corbel et al. 2004; Miller-Jones et al. 2012; Russell et al. 2019).

X-ray emission from black hole binaries (BHBs) shows variability over a broad range of frequencies, and at well defined frequencies (for a recent review, see Ingram & Motta 2019). Quasi-periodic oscillations (QPOs; Van der Klis 1989; Nowak 2000; Belloni et al. 2002) are the narrow peaks in the power density spectrum (PDS). The low-frequency QPOs (LFQPOs) in BHBs can be classified into three classes, namely type A, B, and C, based on the shape of the broadband noise in the PDS, the root mean square (rms) amplitude and phase lags of the QPOs, and the spectral state of the source (Casella et al. 2005; Huang et al. 2018). High-frequency QPOs, with frequency up to ~ 350 Hz, in black holes X-ray binaries are less common (e.g., Morgan et al. 1997; Remillard et al. 1999; Méndez et al. 2013). The dynamic origin of LFQPOs is explained mainly by geometric effects or instabilities in the accretion flow (Stella & Vietri 1998; Tagger & Pellat 1999; Ingram et al. 2009; You et al. 2018; Ma et al. 2021). The radiative properties of QPOs, rms amplitude and phase lags, provide extra information. The 0.1–10 Hz integrated rms amplitude, for instance, is an indicator of accretion regimes in black hole transients (Muñoz-Darias et al. 2011). Type-C QPOs often appear when the source is in the low-hard state and the hard-intermediate state, with central frequency in the range ~ 0.1–15 Hz and associated strong broadband noise in the PDS (Casella et al. 2005). The rms amplitude of the type-C QPOs can increase with energy, and reach $\sim$ 15% at 100 keV (e.g., Huang et al. 2018; Bu et al. 2021), indicating that the radiative mechanism of the type-C QPO has to be related to the corona.

The phase lags are the phase difference of two light curves at different energies in the same frequency range (Nowak et al. 1999). Hard (positive) lags are believed to be due to disc fluctuations that propagate through the corona (Miyamoto et al. 1988), while soft (negative) lags may come from the reprocessing of the hard photons in the disc when the corona illuminates the disc (Lee et al. 2001). The rms spectrum and the phase-lag spectrum of the LFQPOs can indicate how the disc and the Comptonization region influence the evolution of the radiative properties of the LFQPOs (e.g., Reig et al. 2000; Belloni et al. 2005; Zhang et al. 2020a; Kong et al. 2020).

Although the corona around a black hole is widely believed to consist of hot electrons with temperatures up to ~ 100 keV that can give rise to the Comptonized spectrum (Zdziarski et al. 1996; Życki et al. 1999), the geometry of the corona is still under debate (Galeev et al. 1979; Haardt & Maraschi 1991; Poutanen et al. 2018). It is therefore of great significance to determine the geometry of the Comptonization region. Models proposed to constrain the properties of the corona describe either time-averaged energy spectrum or the X-ray variability. For instance, García et al. (2014) proposed a time-averaged reflection model called `relxill` that can measure the height of the corona assuming a lamppost geometry. Using this model You et al. (2021) provided information about how the corona

moves. Ingram et al. (2019) presented a relativistic transfer function model, `reltrans`, that calculates the X-ray time delays and energy shifts based on reverberation mapping. Both these models have been applied to observations (e.g., Xu et al. 2018; Wang et al. 2021), however, neither the time-averaged reflection model nor the reverberation mapping can explain the radiative properties of the QPOs.

Recently, Karpouzas et al. (2020) developed a time-dependent Comptonization model based on the idea proposed by Lee & Miller (1998) and Kumar & Misra (2014). The model of Karpouzas et al. (2020) assumes the QPO to be a sinusoidal coherent oscillation of the Comptonized X-ray spectrum. The oscillation comes from the temperature of the corona, the inner disc, and the external heating source which is necessary to keep the thermal equilibrium of the system. In this model, the corona is assumed to be spherically symmetric and partially covering the accretion disc, while blackbody seed photons from the accretion disc are Compton up-scattered in the corona, leading to hard lags. Since the corona covers the disc to some extent, a fraction of the hard photons in the corona can impinge back onto the accretion disc, resulting in reprocessing of the hard photons and soft lags. The fraction of the feedback photons to the Comptonized photons, ranging from 0 to 1, is called the feedback fraction. The steady-state version of this model describes the Comptonized continuum in the time-averaged energy spectrum, similar, for instance, to `nthcomp` (Zdziarski et al. 1996; Życki et al. 1999), while the time-dependent model can fit simultaneously the fractional rms and phase-lag spectra. The latest version (Bellavita et al., 2022) of the model (Karpouzas et al. 2020) incorporates a disc blackbody as the soft-photon source so the steady-state version of this model is the same as `nthcomp`. Karpouzas et al. (2020) first applied the model to the kilohertz QPOs in the neutron star 4U 1636−53. Later on this model was further applied to the LFQPOs of BHBs: Karpouzas et al. (2021) measured a variable corona in GRS 1915+105 as the frequency of the type-C QPO changes using *RXTE* data; García et al. (2021) applied a dual Comptonization model to the type-B QPO of MAXI J1348+603 with *NICER*, showing that there may be two Comptonization regions near the black hole where the outer region can be the jet. Here we use this time-dependent Comptonization model to study the evolution of the Comptonization region of MAXI J1535−571 through type-C QPOs with *Insight*-HXMT.

MAXI J1535−571 is a new X-ray transient discovered independently by *MAXI*/GSC (Negoro et al. 2017) and *Swift*/BAT (Kennea et al. 2017) on September 2 2017. Follow-up X-ray and radio observations suggested that this new source is a black hole X-ray binary system (Negoro et al. 2017; Russell et al. 2017). Miller et al. (2018) analyzed the *NICER* data and proposed that the black hole spin is 0.994 ± 0.002 and inclination angle is $67.4°\pm0.8°$. A broadband X-ray spectral study also indicated that MAXI J1535−571 has a high spin (> 0.84) and high inclination angle ($\sim 60°$) (Xu et al. 2018). Type-C QPOs were discovered in the low-hard state of MAXI J1535−571, based on *Swift*, *XMM-Newton*, and *NICER* observations (Stiele & Kong 2018). Bhargava et al. (2019) showed a tight correlation between the type-C QPOs and the power-law spectral index, Γ, using *AstroSat* data. Huang et al. (2018) presented a systematic timing study of MAXI J1535−571 with *Insight*-HXMT, classifying different types of LFQPOs and confirming the high inclination angle nature of this system. Using part of the same *Insight*-HXMT dataset where type-C QPOs were detected, Kong et al. (2020) analyzed the energy and fractional rms spectra, and gave a picture of a shrinking and hardening corona. The dataset of MAXI J1535−571 with *Insight*-HXMT provides broadband energy range as well as strong QPO signals that we can utilize to fit with the time-dependent Comptonization model of Karpouzas et al. (2020).

In this paper, we further explore the *Insight*-HXMT observations of MAXI J1535−571 during the outburst in 2017/2018. We fit simultaneously the fractional rms, phase-lag, and time-averaged energy spectra of each observation using the time-dependent Comptonization model of Karpouzas et al. (2020). This paper is organized as follows: In Section 2 we describe the reduction of the *Insight*-HXMT data of MAXI J1535−571, and explain how we generate the power density spectra and the cross spectra for different energy bands. We also explain how we simultaneously fit the fractional rms, lags, and time-averaged energy spectra. In Section 3 we show the temporal evolution of MAXI J1535−571, the dependence of the spectral parameters with QPO frequency and, most importantly, the evolution of the corona. In Section 4 we discuss our results and propose a physical picture to explain the evolution of corona and the possible connection between the corona and the jet.

2 OBSERVATIONS AND DATA ANALYSIS

All observations presented here were carried out with *Insight*-HXMT. The payload of *Insight*-HXMT (Zhang et al. 2014) consists of three instruments: the Low Energy X-ray Telescope (LE), the Medium Energy X-ray Telescope (ME), and the High Energy X-ray Telescope (HE). The LE, ME, and HE cover, respectively, the 1–15 keV energy range with 1 ms time resolution, the 5–30 keV energy range with 240 μs time resolution, and the 20–250 keV energy range with 4 μs time resolution.

Insight-HXMT triggered Target of Opportunity (ToO) observations of MAXI J1535−571 in the period 2017 September 6–23. We use the *Insight*-HXMT Data Analysis Software (HXMTDAS) v2.04 to extract and reduce the data. We use the following criteria to establish the good time intervals (GTIs) to filter the data: we require that the offset of the pointing to the source is less than 0.04° and the source is at least 10° above Earth horizon. To filter out high-background intervals, we make a cut on the geometric cutoff rigidity with COR > 8 GeV, and we select events that are detected at least 300 s before and after the passage of the satellite through the South Atlantic Anomaly (SAA). We finally select all non-blind detectors to generate the products for LE, ME, and HE, respectively.

We use GHATS [1] to compute the Fourier power density spectrum (PDS) of photons in the LE in 1–10 keV energy band, ME in 10–35 keV energy band, and HE in 26–100 keV energy band. We set the time length of each Fast Fourier Transformation (FFT) segment to 25 s and the time resolution to 3 ms so that the lowest frequency of the PDS is 0.04 Hz and the Nyquist frequency is 167 Hz. We average the PDS within one observation, subtract the Poisson level by calculating the average power in the frequency range of > 100 Hz, and normalize the PDS to units of rms^2 per Hz (Belloni & Hasinger 1990). The background count rate used to convert to rms units is estimated with the tools LE(ME/HE)BKGMAP in HXMTDAS. Finally, we apply a logarithmic rebin in frequency to the PDS data such that the size of a bin increases by exp(1/100) compared to that of the previous one.

We use XSPEC v12.11.1 (Arnaud 1996) to fit the PDS with a model consisting of several Lorentzian functions in the frequency range of 0.5–30.0 Hz. Three Lorentzians represent the low-frequency broadband noise, high-frequency broadband noise, and the QPO. Two extra Lorentzians may be needed to represent the harmonic and the subharmonic of the QPO. Following Huang et al. (2018) and Kong

et al. (2020), the eight observations with type-C QPOs in which all the three instruments are active, are selected for further study. Our observations 1–8 correspond to observations in Table 2 of Huang et al. (2018) and Table 3 of Kong et al. (2020); all these observations are in the HIMS. Dynamical power spectra of these observations show that the QPO frequency does not change significantly during an observation. We regard the best-fitting model for each observation as a baseline to perform further fitting on the separate energy bands.

To study the rms spectrum of the QPO, we select the following energy bands, LE: 1.0–2.5 keV, 2.5–3.5 keV, 3.5–5.0 keV, and 5.0–10.0 keV, ME: 10.0–12.0 keV, 12.0–14.0 keV, 14.0–17.0 keV, and 17.0–35.0 keV, HE: 26.0–30.3 keV, 30.3–35.5 keV, 35.5–55.0 keV, and 55.0–100.0 keV. We use the background in the corresponding energy band and use the square root of the normalization of the Lorentzian representing the type-C QPOs to calculate the fractional rms amplitude, hereafter rms (Belloni & Hasinger 1990). To calculate the error of the rms we include the uncertainties of the background count rates.

For each observation, we compute Fourier cross spectra for different energy bands to calculate the phase-lag spectrum of the QPOs (Vaughan & Nowak 1997; Nowak et al. 1999) using the overlapping Good Time Intervals (GTIs) for all the three instruments. The energy bands are the same as for the rms spectra. As we do for the power density spectrum, we use the same time resolution of 3 ms and same time segment of 25 s. We regard the lowest energy band (1.0–2.5 keV) as the reference band. The phase lags of the QPOs are calculated from the average of the real and imaginary parts of the cross spectrum in the frequency range of $\nu_0 \pm$ FWHM/2, where ν_0 is the centroid frequency of the QPOs. A positive lag means that the hard photons lag the soft ones.

2.1 Fitting the time-averaged, rms, and phase-lag spectra separately

We use XSPEC v12.11.1 (Arnaud 1996) to fit the time-averaged, rms, and phase-lag spectra. We adopt the energy bands 2–10 keV (LE), 10–35 keV (ME), and 26-100 keV (HE) for the fitting of the time-averaged spectrum, adding a systematic error of 1%. Since we assume that the variability at the QPO frequency comes from the corona, we fit the time-averaged and the time-dependent spectra using the same model in which we consider the Comptonization of the seed photons from the accretion disc as the component that drives the variability. We start by fitting the time-averaged spectrum in each observation with the model const*tbabs*(diskbb+nthcomp), where the multiplicative constant is used to account for cross-calibration uncertainties between three instruments. In the absorption model tbabs, the parameter N_H represents the hydrogen column density, with the cross-section and solar-abundance tables of Verner et al. (1996) and Wilms et al. (2000), respectively. To fit the emission of the accretion disc, we use diskbb (Mitsuda et al. 1984), which has two parameters: the inner disc temperature, kT_{in}, and a normalization. To fit the hard Comptonized continuum, we use nthcomp (Zdziarski et al. 1996; Życki et al. 1999), which has the following parameters: the corona temperature, kT_e, the X-ray photon index, Γ, the seed photon temperature, kT_s, and a normalization. We assume that the seed photon source is the disc so when performing the fitting the kT_{in} in diskbb and kT_s in nthcomp are linked.

Fits with the model const*tbabs*(diskbb+nthcomp) show residuals at ∼ 6–7 keV and ∼ 20–30 keV, suggesting that there may exist a reflection component (e.g., Xu et al. 2018; Jiang et al. 2020). We therefore add a relativistic reflection component, relxillCp (García et al. 2014), to the model that now is

`const*tbabs*(diskbb+nthcomp+relxillCp)`. We link kT_e and Γ in `relxillCp` to kT_e and Γ in `nthcomp` and, as before, kT_s in `nthcomp` to kT_{in} in `diskbb`. In `relxillCp`, the black hole spin, a_*, inclination angle, i, disc inner radius, R_{in}, logarithm of the ionization parameter, $\log\xi$, iron abundance, A_{Fe}, and normalization of the model are free during the fits, whereas the reflection fraction is fixed at -1 since we only consider the reflected emission (the direct emission is given by `nthcomp`); we also link the emissivity indices q_1 and q_2 during the fits.

To fit the rms and phase-lag spectra, we utilize the model of [Karpouzas et al. (2020)](#) with a disc blackbody spectrum for the seed-photon source (Bellavita et al. 2022), which we call `vkompthdk` in this paper. Since both `vkompthdk` and `nthcomp` come from the same calculation of the Comptonization spectrum, the time-averaged version of `vkompthdk` is the same as `nthcomp`, and both models share the same parameters. However, the time-dependent version of `vkompthdk` has extra parameters, namely the size of the corona, L, feedback fraction, η, amplitude of the variability of the external heating rate, $\delta\dot{H}_{ext}$, QPO frequency and a reference lag. The reference lag is an additive parameter that accounts for the fact that the reference band of the lags is arbitrary, and hence the lag spectrum can be shifted up and down arbitrarily (e.g., [García et al. 2021](#)).

2.2 A joint fitting

Since our aim is to fit the rms, phase-lag, and time-averaged spectra simultaneously, we use `vkompthdk` instead of `nthcomp` to fit the three spectra given that the time-averaged version of `vkompthdk` is the same as `nthcomp`. We therefore fit jointly the three spectra in each observation where the energy ranges we use per instrument are 1–10 keV, 10–35 keV, and 26–100 keV for the rms and phase-lag spectra, and 2–10 keV, 10–35 keV, and 26–100 keV for the time-averaged spectra. The model that we use is written as `const*tbabs*(diskbb+vkompthdk+relxillCp)`. We let N_H and the normalizations of `diskbb` and `relxillCp` free to fit the time-averaged spectrum, while we fix all of them at 0 to fit the rms and phase-lag spectra. For `vkompthdk` the normalization is free when fitting the time-averaged spectrum and fixed at 1 for the rms and phase-lag spectra (see [García et al. 2021](#)). Besides these parameters, the other parameters that are always free are: kT_{in} in `diskbb`, kT_e and Γ in the time-averaged version of `vkompthdk`, where kT_s in `vkompthdk` is linked to kT_{in} in `diskbb`, q_1, a_*, i, R_{in}, $\log\xi$, and A_{Fe} in `relxillCp`, where kT_e and Γ in `relxillCp` are linked to the same parameters in `vkompthdk`. The reflection fraction is fixed to -1 so that `relxillCp` only provides the reflected component, while `vkompthdk` provides the direct emission from the hard Comptonization component. When we use the time-dependent version of `vkompthdk` to fit the rms and phase-lag spectra, the QPO frequency is fixed at the frequency of the QPO in the PDS in each observation, while L, η, $\delta\dot{H}_{ext}$ and the reference lag, which act only on the phase-lag spectrum as mentioned in [2.1](#), are free.

We fit the data from the three instruments, i.e. LE, ME, and HE, simultaneously, so in each observation we have three time-averaged, three rms and three phase-lag spectra, respectively, and the parameters in the model of each component are linked across different instruments. Initially the spin, a_*, and the inclination angle, i, in the reflection model are free to change from one observation to the other. However, we notice that these parameters are high and more or less constant when the QPO frequencies are low, but drop when the QPO frequencies are high. [Miller et al. (2018)](#) and [Xu et al. (2018)](#) suggested a high spin (> 0.84) and a high inclination angle ($> 60°$) for MAXI J1535−571. Since in principle these parameters should

not change from one observation to the other, we fix the spin and inclination angle at the average values of all our fits, i.e. 0.998 and 60.2°, respectively. In the fits the hydrogen column density N_H is also fixed at the average value obtained from the fits of the eight observations.

3 RESULTS

3.1 The light curve and HID of MAXI J1535−571

In the left panel of Figure [1](#) we show the MAXI light curve of MAXI J1535−571 in the 2–20 keV band during the 2017/2018 outburst, from MJD 57918 to MJD 58312. The X-ray emission of MAXI J1535−571 is undetectable until ∼ MJD 58000. From that date onwards the source displays a rise up to a maximum intensity of ∼ 7 counts cm^{-2} s^{-1} on MJD 58016, and after that it decays gradually. The vertical dashed lines in Figure [1](#) show that the *Insight*-HXMT observations of MAXI J1535−571 only cover part of the full outburst, especially the rising phase and the end of the outburst. [Huang et al. (2018)](#) reported the type-C QPOs detected by *Insight*-HXMT in the intermediate state of the source. Those observations are marked with red dashed lines in Figure [1](#). Radio observations of MAXI J1535−571 start from MJD 58000 until just after MJD 58050, covering the whole intermediate states of the source ([Russell et al. 2019](#); [Chauhan et al. 2021](#)).

The MAXI hardness intensity diagram (HID) of MAXI J1535−571 in the right panel of Figure [1](#) shows that the source traces the characteristic 'q' path, which is typical for other black hole transients ([Fender et al. 2004](#)). During the transition to the high-soft state, the hardness ratio drops as the count rate increases. *Insight*-HXMT observations after the intermediate state show that the source goes into a low-luminosity state. We also plot in red the eight observations with type-C QPOs that we analyze in detail in this paper. As shown in Table [1](#), according to the classification by [Huang et al. (2018)](#), observations 1–5 were in the hard-intermediate state (HIMS), while observations 6–8 were in the soft-intermediate state (SIMS). We note, however, that the presence of a type-C QPO in those observations, also classified as such by [Huang et al. (2018)](#), indicates that the source was instead in the HIMS. [Huang et al. (2018)](#) found a type-B QPO, which is part of the definition of the SIMS, in observation 701, between the first five and the last three observations in our sample. This indicates that during the first five observations in our sample the source was in the HIMS, it went briefly into the SIMS in observation 701 of [Huang et al. (2018,](#) this observation is not included in our sample), and then went back to the HIMS in observations 901–903 in our sample. Note that in the right panel of Figure [1](#) a blue point (obs ID P011453500601) between the red points corresponds also to an observation in the intermediate state with type-C QPOs. However we exclude this observation since the GTIs of LE, ME, and HE do not overlap and thus we cannot compute the phase-lag spectrum of this observation.

3.2 Joint fits of the rms, phase-lag, and time-averaged spectra

In Table [1](#) we show the *Insight*-HXMT observation IDs of MAXI J1535−571 with type-C QPOs; the QPO frequency is in the range of 2.12–9.02 Hz, and the source is in the intermediate state. Our classification of the QPOs as type-C QPOs is consistent with the classification in these observations by [Huang et al. (2018)](#) although, as we mentioned above, [Huang et al. (2018)](#) misclassified the state of the source in the last three observations presented here. From MJD
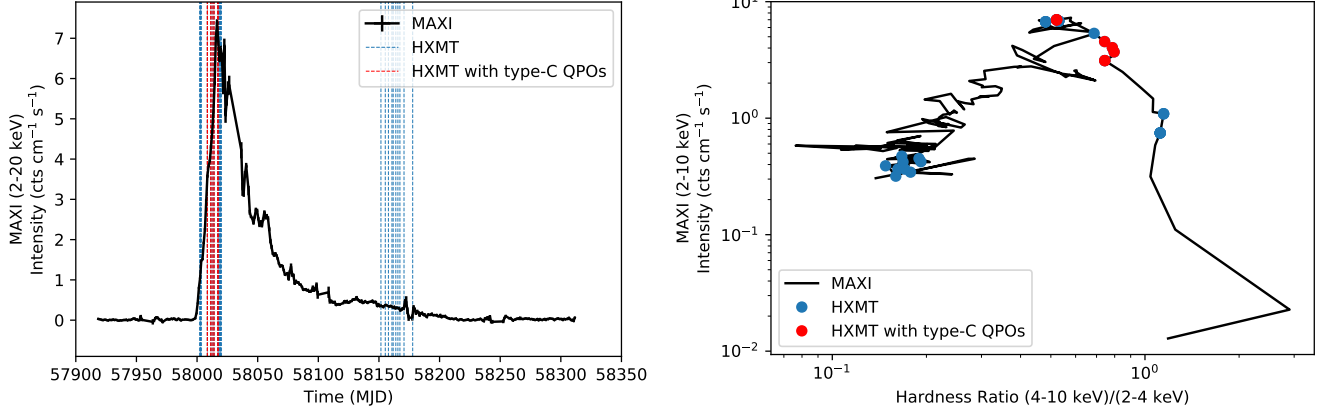
Figure 1. Left panel: MAXI light curve of MAXI J1535−571 in black with the time of all the *Insight*-HXMT observations indicated by the vertical dashed lines. The selected MJD range of MAXI observations is from 57918 to 58312. The red dashed lines represent the observations that we analyze with type-C QPOs in the intermediate state. Right panel: Hardness intensity diagram (HID) of MAXI J1535−571 using MAXI data in black. The selected MJD range of MAXI observations is from 57997 to 58174. The blue and red points indicate the simultaneous *Insight*-HXMT observations. The red points represent the observations that we analyze with type-C QPOs in the intermediate state. Note that some of the red points overlap each other. There are 3 red points in the left group and 5 red points in the right group.
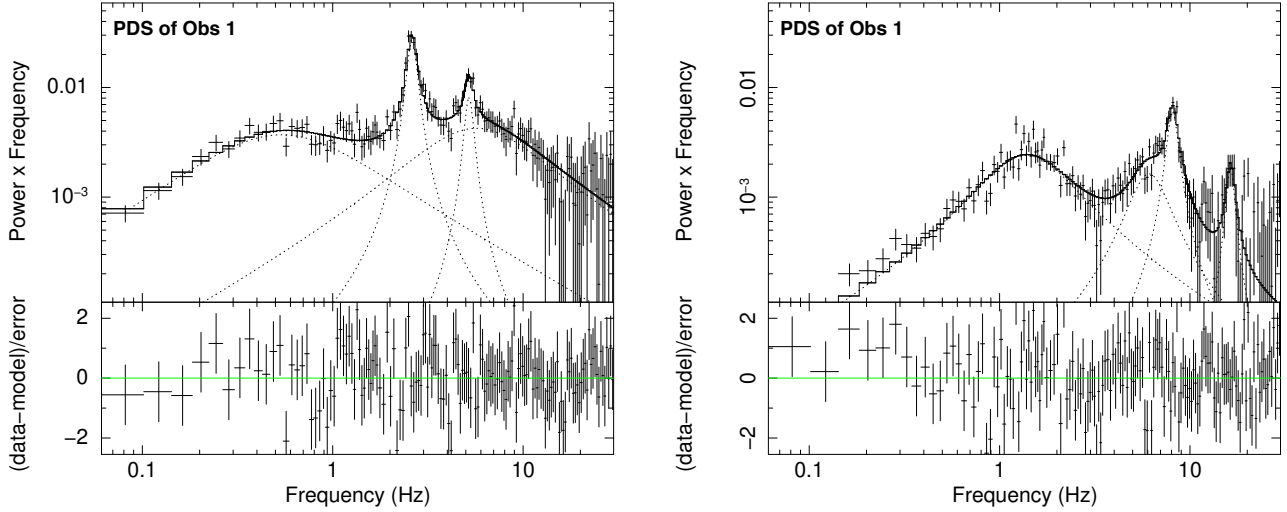

Figure 2. Two representative PDS of MAXI J1535−571 using the 1–10 keV LE data of *Insight*-HXMT . Left panel: The PDS (top) and the best-fit residuals (bottom) of Obs 1. Right panel: The PDS (top) and the best-fit residuals (bottom) of Obs 8.

Table 1. Observations and QPOs of MAXI J1535−571. The error bar indicates the 90% confidence level. Each observation ID has a prefix of P011453500.

	Obs IDs	MJD	QPO Frequency (Hz)	FWHM
Obs 1	144	58008.44	2.61 ± 0.02	0.32 ± 0.06
Obs 2	145	58008.58	2.58 ± 0.02	0.63 ± 0.05
Obs 3	301	58011.20	2.12 ± 0.02	0.35 ± 0.10
Obs 4	401	58012.26	2.73 ± 0.02	0.29 ± 0.06
Obs 5	501	58013.26	3.34 ± 0.02	0.39 ± 0.05
Obs 6	901	58017.10	8.88 ± 0.08	0.93 ± 0.19
Obs 7	902	58017.25	9.02 ± 0.06	1.04 ± 0.19
Obs 8	903	58017.39	8.08 ± 0.11	1.04 ± 0.34

58008 to MJD 58013, when the type-C QPO frequency decreases from 2.61 Hz to 2.12 Hz and then increases to 3.34 Hz, the source is in the HIMS. According to Huang et al. (2018), on MJD 58015 a

type-B QPO is detected, which indicates that on this date the source is in the SIMS. (Notice that we do not include this observation and this QPO in our analysis.) Finally, the three observations on MJD 58017 contain again a type-C QPO with a frequency that shows a fast increase from 3.34 Hz to around 9 Hz. The presence of the type-C QPO indicates that, after a short excursion, the source is again in the HIMS. The variable frequency of the type-C QPOs in the HIMS is consistent with the measurements of Bhargava et al. (2019) who had a much better time sampling. The left panel of Figure 2 shows the PDS of observation 1, while the right panel shows the PDS of observation 8. Both panels display a strong signal of the type-C QPOs and the harmonics. In the first and third panels of Figure 3 we plot the rms, phase-lag, and time-averaged spectra when the QPO frequencies are 2.61 Hz and 8.08 Hz, while the second and fourth panels show the residuals to the best-fitting model. When the QPO frequency is 2.61 Hz, the rms first increases with energy and gradually flattens
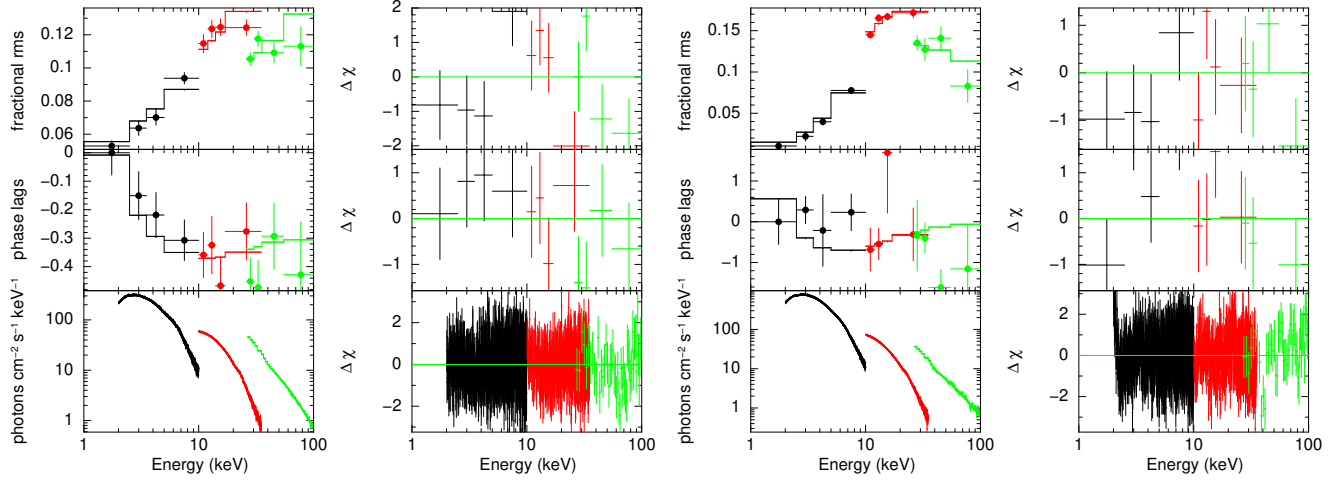
Figure 3. Two representative rms (top panel), phase-lag (middle panel), and time-averaged (bottom panel) spectra with joint fitting of MAXI J1535−571 using *Insight*-HXMT. The first panel shows the spectra for Obs 1 (QPO frequency 2.6 Hz), while the second panel shows the residuals with respect to the best-fitting model. The third and fourth panels show the same for Obs 8 (QPO frequency 8.1 Hz). The black, red, and green colors indicate the LE, ME, and HE data of *Insight*-HXMT, respectively.

Table 2. Best-fitting spectral parameters for the model `tbabs*(diskbb+vkompthdk+relxillCp)` used to fit the data of MAXI J1535−571. The error bars indicate the 90% confidence level.

	Obs 1	Obs 2	Obs 3	Obs 4	Obs 5	Obs 6	Obs 7	Obs 8
$N_{\rm H}$ (10^{22})	5.553*	5.553*	5.553*	5.553*	5.553*	5.553*	5.553*	5.553*
$kT_{\rm s}$ (keV)	0.27 ± 0.03	0.23 ± 0.02	0.24 ± 0.01	0.21 ± 0.05	0.23 ± 0.05	0.78 ± 0.06	0.70 ± 0.05	0.71 ± 0.04
$\rm Norm_{disc}$ (10^3)	1700^{+2500}_{-1000}	5900^{+9800}_{-3100}	5500^{+1700}_{-1300}	$16000^{+192000}_{-10000}$	3600^{+33100}_{-3100}	$7.4^{+2.1}_{-1.6}$	13 ± 3	$8.3^{+1.5}_{-2.6}$
Γ	2.49 ± 0.03	2.49 ± 0.01	2.43 ± 0.02	2.59 ± 0.02	2.60 ± 0.02	$2.83^{+0.02}_{-0.05}$	2.88 ± 0.02	2.80 ± 0.02
$kT_{\rm e}$ (keV)	32 ± 3	34 ± 2	34 ± 2	44^{+8}_{-4}	39 ± 3	202^{+44}_{-53}	250_{-40}	250_{-48}
q_1	$8.1^{+1.8}_{-1.3}$	$9.7^{+(P)}_{-1.1}$	6.0 ± 0.3	6.1 ± 0.2	5.9 ± 0.2	8.4 ± 0.4	8.9 ± 0.2	8.7 ± 0.3
a_*	0.998*	0.998*	0.998*	0.998*	0.998*	0.998*	0.998*	0.998*
i (°)	60.2*	60.2*	60.2*	60.2*	60.2*	60.2*	60.2*	60.2*
$R_{\rm in}$ (ISCO)	1.64 ± 0.06	1.66 ± 0.03	$1.00^{+0.06}$	$1.00^{+0.28}$	$1.00^{+0.06}$	1.08 ± 0.02	1.08 ± 0.01	1.07 ± 0.02
$\log \xi$	$2.83^{+0.26}_{-0.07}$	2.89 ± 0.07	$2.86^{+0.07}_{-0.11}$	2.7 ± 0.1	$3.09^{+0.08}_{-0.05}$	$4.70_{-0.04}$	$4.70_{-0.03}$	$4.6^{+(P)}_{-0.1}$
$A_{\rm Fe}$	$0.95^{+0.75}_{-0.12}$	0.58 ± 0.06	$0.51^{+0.11}_{-0.01}$	0.72 ± 0.09	$0.88^{+0.08}_{-0.11}$	2.1 ± 0.3	$3.2^{+1.0}_{-0.3}$	2.0 ± 0.2
$\rm Norm_{refl}$	0.53 ± 0.09	0.60 ± 0.05	1.1 ± 0.1	1.8 ± 0.3	1.7 ± 0.1	3.3 ± 0.2	3.0 ± 0.2	3.2 ± 0.2
L $(10^3$ km)	5.1 ± 2.0	4.4 ± 1.2	3.4 ± 0.4	3.0 ± 0.9	$3.2^{+0.3}_{-0.6}$	$5.5^{+1.2}_{-0.9}$	4.6 ± 0.7	$6.9^{+1.5}_{-1.2}$
η	$0.85^{+0.13}_{-0.10}$	0.74 ± 0.06	0.77 ± 0.05	0.90 ± 0.05	$0.96^{+(P)}_{-0.04}$	$0.54^{+0.18}_{-0.15}$	0.48 ± 0.16	$0.78^{+(P)}_{-0.26}$
$\delta \dot{H}_{\rm ext}$	0.085 ± 0.007	0.097 ± 0.004	0.0817 ± 0.003	0.072 ± 0.004	0.077 ± 0.007	0.089 ± 0.015	0.095 ± 0.006	0.13 ± 0.02
$\rm Norm_{Comp}$	$0.23^{+0.20}_{-0.12}$	$0.53^{+0.35}_{-0.19}$	0.51 ± 0.06	$2.5^{+1.9}_{-1.3}$	1.5 ± 1.0	$0.014^{+0.013}_{-0.006}$	0.045 ± 0.021	$0.025^{+0.015}_{-0.009}$
χ^2/ν	1194.8/1426	1284.8/1426	1415.4/1426	1358.0/1426	1484.7/1426	1404.8/1426	1381.6/1426	1330.6/1426

[1] The letter (P) indicates that the positive 90% error of the parameter pegged at the upper boundary.

above 10 keV, while the phase lags are always negative (soft) and their magnitude increases with energy. When the QPO frequency is 8.08 Hz, the rms increases with energy, gradually flattens above 10 keV, and drops slightly above 30 keV, while the phase lags are negative and more or less constant with energy, but with larger error bars than in the case when the QPO frequency is at 2.61 Hz. The fact that the lags are soft indicates that soft photons emitted by the disc might be largely due to hard photons from the illuminating corona after being reprocessed (Lee et al. 2001; Karpouzas et al. 2020).

We fit the rms, phase-lag, time-averaged spectra jointly using the method described in Section 2.2. As an example, Figure 3 shows the best-fitting model to the rms, phase-lag, and time-averaged spectra when the QPO frequency is 2.61 Hz (first panel, with residuals in the second panel) and 8.08 Hz (third panel, with residuals in the fourth panel).

In observations 1–5, when the QPO frequency is in the range of 2.12–3.34 Hz, the power-law index of the Comptonized component in the time-averaged spectrum is in the range of 2.4–2.6 and the disc

temperature is around 0.3 keV, while in the observations 6–8, when the QPO frequency is about 9 Hz the power law is steeper, with $\Gamma \sim 2.8$, and the temperature of the disc increases to ~ 1.0 keV (see Figure 4 and Table 2). In observations 1–5 the temperature of the corona is $kT_{\rm e} \sim 40$ keV, whereas in observations 6–8 $kT_{\rm e}$ changes quickly and reaches the upper limit of 250 keV that we set in the fits. The change of the values of spectral parameters in the time-averaged spectrum indicates that MAXI J1535−571 may be about to undergo a state transition from the HIMS to the SIMS. The normalization of the disc component, $\rm Norm_{disc}$, decreases as the temperature of the disc, $kT_{\rm s}$, increases; this anti-correlation is consistent with the findings of Tao et al. (2018). The emissivity index, q_1, in the `relxillCp` component is usually larger than 6, indicating that the corona is close to the black hole (García et al. 2014, 2018) or the radial dependence of the disc ionization state (Svoboda et al. 2012). The best-fitting values of the inner radius of the accretion disc, $R_{\rm in}$, are consistent with the innermost stable circular orbit (ISCO), which suggests that the inner disc is stable from MJD 58008 to MJD 58017. In the HIMS,

the logarithm of the disc ionization parameter is around 3 and the iron abundance is less than that of the Sun; in the late stage of the HIMS, the disc is more ionized with the ionization parameter increasing by an order of the magnitude and the best-fitting iron abundance is around 2 times the solar abundance.

3.3 The evolution of the geometry of the corona

In Figure 4 we show the evolution of the size of the corona, L, the feedback fraction, η, and the amplitude of the variability of the external heating rate, $\delta \dot{H}_{ext}$, obtained from the time-dependent version of the model vkompthdk that fits the rms and phase-lag spectra. As the frequency of the type-C QPO increases from 2.12 Hz to 3.34 Hz, the size of the corona decreases from 5100 km to 3200 km. At the same time the feedback fraction remains broadly constant in the range of 0.7–1. When the QPO frequency increases further, from 3.34 Hz to 9.02 Hz, the feedback fraction decreases to around 0.5 as the size of the corona increases from 3200 km to around 5500 km. The amplitude of the variability of the external heating rate shows the same evolution trend as the size of the corona. The Lense-Thirring radius (Ingram et al. 2009), calculated from the QPO frequency assuming a black hole mass of 10 $M_{\odot}$ (Sridhar et al. 2019) and a spin of 0.998, goes from 200 km to 100 km as the QPO frequency evolves from 2 Hz to 9 Hz. These radii are well below the size of the corona, which suggests that the corona always covers a large fraction of the inner disc, consistent with the relatively large values of η.

If we order the size of the corona and feedback fraction according to time (see Table 2 and Figure 5), in observations 1–5 the size of the corona starts at 5100 km, then decreases to 3200 km while, at the same time, the feedback fraction first decreases slightly from 0.85 to 0.74, and then increases marginally and stays at values larger than 0.9. In observations 5–8 the corona size increases from 3200 km to around 5500 km, while the feedback fraction decreases from 0.96 to around 0.5.

Using *NICER* data, Rawat et al. (2022) found that the relation of the time lags of the QPO between two broad energy bands, the spectral parameters of the source, kT_s, and Γ, the corona size L and the feedback fraction η vs. QPO frequency show a statistically significant break at a QPO frequency $\nu_c = 3.5$ Hz. (Because of *NICER*'s lack of high-energy coverage, different from us they could not measure kT_e in their data.) To explore this in our observations, we first fit each relation in Figure 4 independently with either a straight or a broken line. Since in the latter fits the values of the break frequency, ν_c, of the individual fits are consistent with each other within the 3-σ errors, we fit all the relation again simultaneously, this time linking the break frequency of all fits. Differently from Rawat et al. (2022), we find that since the F-test probability is 0.03, the fit with a broken line is only marginally better than that with a straight line, possibly due to the fact that we have no observation with QPO frequency in the range of 4–8 Hz. Our best-fitting broken line gives $\nu_c = 3.25^{+0.60}_{-0.21}$ Hz, consistent with the value found by Rawat el al. (2022). We also fit a broken power-law instead of broken line to the size of the corona and the external heating rate vs. QPO frequency, however, the reduced χ^2 and the break frequency do not change significantly compared to the fits with a broken line.

4 DISCUSSION

We have analyzed all the observations of the 2017/2018 outburst of MAXI J1535−571 with *Insight*-HXMT up to 100 keV. The light curve and 'q' path in the HID (Figure 1) show that MAXI J1535−571

behaves like a typical black hole X-ray transient. We find that the temperature of the disc and the photon index of the hard Comptonized component increase with time, indicating a softening of the source spectrum as the source moves along the HIMS. At the same time the inner radius of the accretion disc remains rather stable. We jointly fit the time-averaged, rms and phase-lag spectra of the QPO of eight *Insight*-HXMT observations of MAXI J1535−571 with type-C QPOs; the frequency of the QPO ranges from 2.12 Hz to 9.02 Hz during the HIMS. As shown in Figure 4, as the frequency of the type-C QPO increases, the size of the corona, L, and the amplitude of the variability of the external heating rate, $\delta \dot{H}_{ext}$, decrease and then increase slightly. At the same time the feedback fraction, η, does the opposite.

Previous studies have reported the evolution of the physical parameters of MAXI J1535−571, e.g., spin of the black hole, inclination angle of the accretion disc, and height of the corona. For instance, Huang et al. (2018) analyzed the *Insight*-HXMT observations, some of which we present in this paper, and concluded that the system inclination angle must be high, judging from the soft lags of the type-C QPOs. From fits to the time-averaged spectra with the reflection model rexilllpCp, Xu et al. (2018) reported a high spin and a corona that is very close to the black hole in the low hard state. Miller et al. (2018) used relxill to deduce a high spin and a high emissivity index, which also indicates that the corona is close to the black hole. All of these authors concluded that the inclination angle of MAXI J1535−571 is high. However, the spectral analysis mentioned before just focus on one observation of *NuSTAR* or *NICER*. In the hard/soft intermediate state, we use the relxillCp model to fit eight observations, showing an average spin of 0.998 and inclination angle of 60.2°. Our fits show that the emissivity index is large (> 6), indicating a corona close to black hole (Wilkins & Fabian 2012) or a radial dependence of the disc ionization during these observations (Svoboda et al. 2012). The time-dependent Comptonization model vkompthdk requires a large corona to explain the lags of the photons. If the corona is large, the radial change of the disc ionization profile could be responsible for the high value of the emissivity index in MAXI J1535−571.

In an outburst of a BHB, as the disc emission increases during the softening of the spectrum in the LHS and HIMS (e.g., Méndez & van der Klis 1997; Huang et al. 2018; Zhang et al. 2020b), the rate at which the corona cools down due to inverse-Compton scattering would increase. The temperature of the corona, and hence the energy at which the spectrum cuts off at high energies, may either decrease or increase, depending on the balance between the inverse-Compton cooling and the mechanism that heats up the corona (Merloni & Fabian 2001; Karpouzas et al. 2020). Our results show that during the HIMS, the high-energy cutoff increases from 32 keV to at least 250 keV. This trend is the same as the ones shown in Joinet et al. (2008), Del Santo et al. (2008) and Motta et al. (2009). Del Santo et al. (2008) showed this phenomenology in the HIMS data of GRO J1655−40 with INTEGRAL, which displays a non-thermal hard tail at high energy. This tail becomes more dominant and the high-energy cutoff increases when the source is about to transit into the soft state. Similarly, Motta et al. (2009) showed that in the case of GX 339−4 the power-law cutoff energy first decreases as the source moves in the LHS and HIMS, and increases again just before the transition to the SIMS. The evolution of the power-law cutoff energy in these two sources is consistent with the behavior of the corona temperature that we report here for MAXI J1535−571 in the HIMS.

In the framework of Lense-Thirring (LT) precession as the explanation of the dynamical origin of the type-C QPOs, Ingram et al. (2009) assumed that a torus-like corona precesses within the inner radius of a truncated disc (see also, You et al. 2018). Assuming that
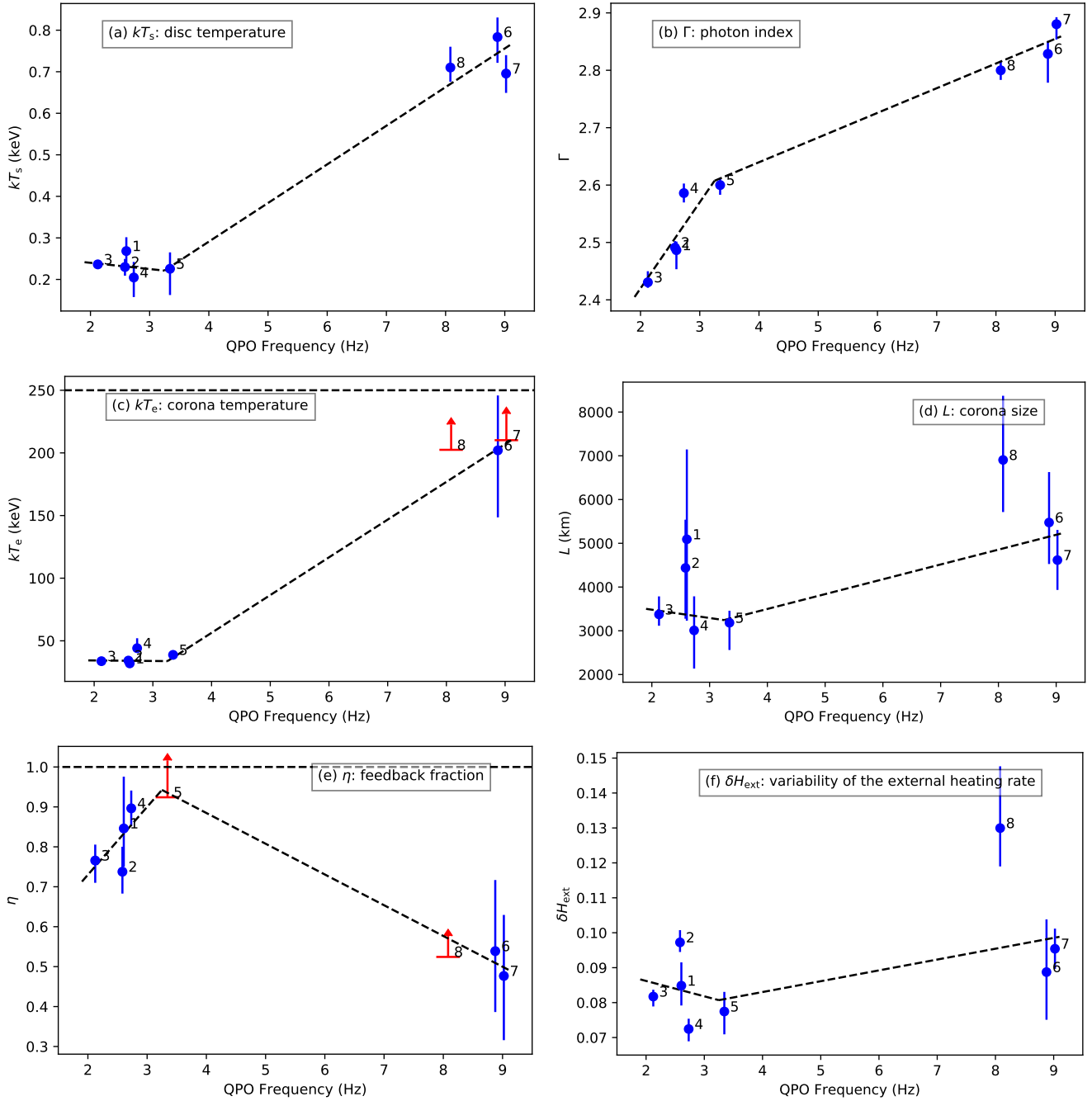
Figure 4. The evolution of the parameters of MAXI J1535−571 vs. QPO frequency. The parameters are, respectively, (a) disc temperature, kT_s, (b) photon index, Γ, (c) corona temperature, kT_e, (d) corona size, L, (e) feedback fraction, η, and (f) variability of the external heating rate, $\delta\dot{H}_{ext}$. The error bars represent the 90% confidence level, while red points show 95% lower limits. Black dashed broken line is the best fit to the data by a broken line with a break frequency at 3.25 Hz. The numbers on each panel indicate the observations in Table 1. The horizontal black dashed lines in panels (c) and (e) are the upper boundary of 250 keV and 1, respectively.

the mass of the black hole in MAXI J1535−571 is $10M_\odot$ (Sridhar et al. 2019) and the spin is 0.998 from our fits, the LT radius decreases from 200 km to 100 km as the QPO frequency increases from 2 Hz to 9 Hz. The LT radius is much smaller than the corona size we obtain from our fits, the minimum of which is around 3000 km. The time-dependent Comptonization model (Karpouzas et al. 2020) that we use does not explain the dynamical origin of the QPO, but only requires that there is a coupled oscillation of the physical quantities:

corona temperature, kT_e, temperature of the inner accretion disc, kT_s, external heating rate, $\delta\dot{H}_{ext}$, and the time-dependent photon number density that is dynamically scattering in the plasma. We favor the scenario in which the inner disc oscillates since, if the source of soft photons precesses, the line-of-sight soft photons oscillate and would potentially cause a perturbation in the corona temperature.

Assuming that the time lags of the broadband noise component are due to reverberation, Kara et al. (2019) concluded that the corona
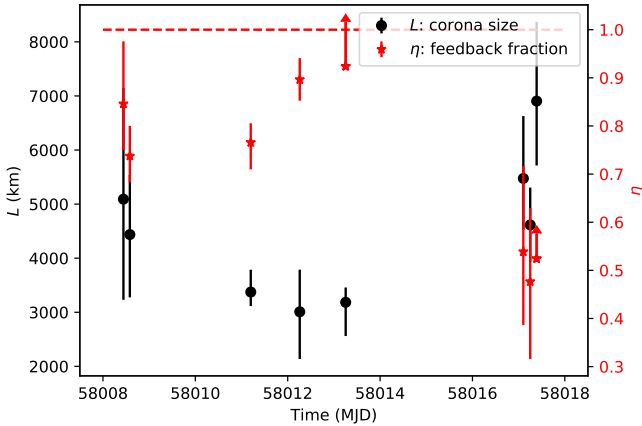
Figure 5. Temporal evolution of the corona size L (black) and the feedback fraction η (red) of MAXI J1535−571. The arrow in the point means the lower limit of the measurement. The red horizontal dashed line is the upper limit of 1, according to the definition of the time-dependent Comptonization model.

of MAXI J1820+070 contracts as the source is in the low-hard state. Wang et al. (2021) proposed that the source expands again when evolving further in the intermediate state. Using the time-dependent Comptonization model, Karpouzas et al. (2021) showed that in GRS 1915+105 the size of the corona first decreases from 10000 km to 100 km and then increases to 1000 km as the QPO frequency increases from 0.5 Hz to 6 Hz, while the feedback fraction increases monotonically (see also Méndez et al. 2022). Our result of the size of the corona shows the same trend in MAXI J1535−571 as that in GRS 1915+105, but the size of the corona in the case of MAXI J1535−571 is about one order of magnitude larger than in GRS 1915+105. In MAXI J1535−571, different from GRS 1915+105 the feedback fraction first remains broadly constant in the range of 0.7–1 and then decreases as the QPO frequency increases, providing a different picture of the evolution of the corona.

Similar to the case of GRS 1915+105 (Méndez et al. 2022), the large size of the corona in MAXI J1535−571 indicates that the corona would cover the disc beyond the inner radius. However, at the same time that the corona is large, the feedback fraction is small. This suggests that the corona is not spherical, but extends perpendicularly to the accretion disc. In these conditions the assumption of a spherical corona in the model of Karpouzas et al. (2020) would not be satisfied. In this case L must therefore represent a characteristic size of the corona such that the magnitude of the predicted lags can match the observed ones (see Méndez et al. 2022).

Our results of the temporal evolution of the corona may be compared to the evolution of the radio jet detected in this source. Radio measurements (Russell et al. 2019, 2020; Chauhan et al. 2021) show that during the intermediate state of MAXI J1535−571 a steady, optically thick jet gradually quenches and then changes into a transient jet. More specifically, on MJD 58008, the radio observations detect a steady, optically thick jet. On MJD 58013 the radio emission weakens and the jet is quenched. On MJD 58017, the radio emission reappears, but this time the spectrum is optically thin, indicating a transient jet with discrete ejecta.

Based on our results and the radio measurements of Russell et al. (2019) and Chauhan et al. (2021), in Figure 6, we present schematically a possible scenario of the evolution of the X-ray corona and the simultaneous radio jet. The parameters from the reflection suggest a rather stable inner radius of the disc that is very close to the ISCO,

so the disc inner radius does not change significantly in Figure 6. Initially, the QPO frequency is 2.61 Hz, and the size of the corona is 5100 km. When the QPO frequency first decreases from 2.61 Hz to 2.12 Hz, the corona size decreases from 5100 km to 3400 km and the feedback fraction decreases slightly from 0.85 to 0.77 in the time period from MJD 58008 to MJD 58011 (Figure 5). As the QPO frequency increases from 2.12 Hz to 3.34 Hz, the corona size remains constant at around 3000–3400 km. Since the feedback fraction increases from 0.77 to 0.96, suggesting that the corona covers a larger part of the disc, the corona should expand along the horizontal direction but contract along the vertical direction. This phase corresponds to the time period from MJD 58011 to MJD 58013. In the period MJD 58013–58017, the QPO changes from 3.34 Hz to 8.08 Hz and the corona expands again. Since in this phase the feedback fraction decreases from 0.96 to ∼ 0.5, indicating that a smaller part of the disc is covered by the corona, the expansion of the corona must be along the vertical direction.

Using different approaches, a similar evolution of the corona has been reported. Using the reflection model `relxillCp` (García et al. 2014) to fit the *Insight*-HXMT data, You et al. (2021) found that the corona in MAXI J1820+070 outflows faster when it moves closer to the black hole, which suggests a jet-like corona and that the jet gains energy as the corona outflows. Utilizing the `reltrans` model (Ingram et al. 2019) to fit the broadband time-lag spectra, Wang et al. (2021) found a connection between the corona and the jet in the intermediate state of MAXI J1820+070. The picture proposed by Wang et al. (2021) is in agreement with ours: The quenching of the steady jet follows the contraction of the corona, while the transient jet appears after the expansion of the corona. More observations and spectral modelling using the time-dependent Comptonization model in the future would provide a complete picture of the corona-jet evolution, and the role of the disc during this evolution.

DATA AVAILABILITY

The data used in this article are accessible at the *Insight*-HXMT website http://hxmtweb.ihep.ac.cn.
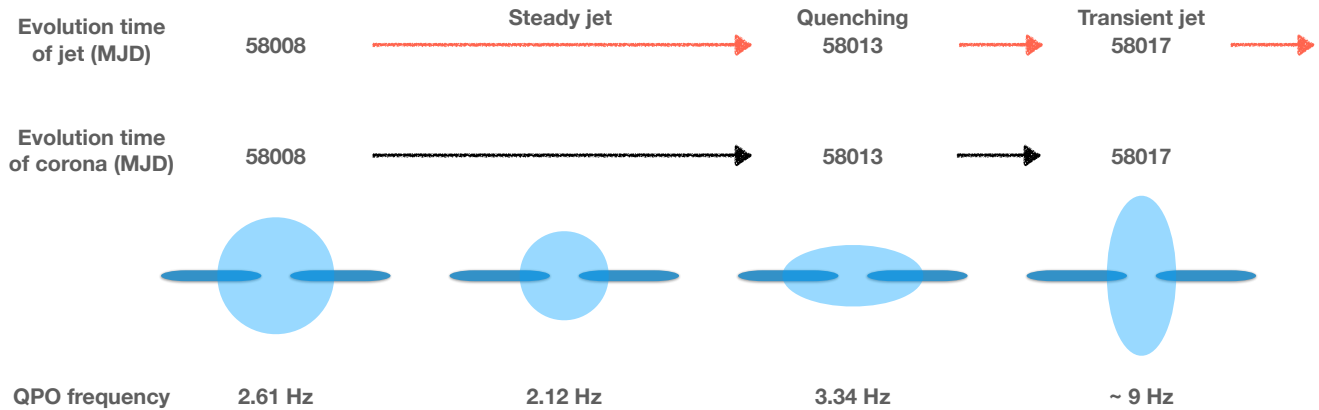
Figure 6. Schematic figure illustrating the time evolution of the corona and the jet of MAXI J1535−571 (see text for a more detailed explanation). From MJD 58008 to MJD 58011 the size of the corona contracts; from MJD 58011 to MJD 58013 the corona contracts vertically but expands horizontally. In the period before MJD 58013 the radio spectrum of the source is consistent with optically thick synchrotron emission from a compact steady jet and on MJD 58013 the jet is quenched. From MJD 58013 to MJD 58017 the corona expands vertically but contracts horizontally and after MJD 58017 the radio data are consistent with optically thin synchrotron emission from a transient jet.

REFERENCES

Arnaud K. A., 1996, in Jacoby G. H., Barnes J., eds, Astronomical Society of the Pacific Conference Series Vol. 101, Astronomical Data Analysis Software and Systems V. p. 17

Bambi C., et al., 2021, Space Sci. Rev., 217, 65

Bellavita C., et al., 2022, in prep

Belloni T., Hasinger G., 1990, A&A, 230, 103

Belloni T., Psaltis D., van der Klis M., 2002, ApJ, 572, 392

Belloni T., Homan J., Casella P., van der Klis M., Nespoli E., Lewin W. H. G., Miller J. M., Méndez M., 2005, A&A, 440, 207

Bhargava Y., Belloni T., Bhattacharya D., Misra R., 2019, MNRAS, 488, 720

Bu Q. C., et al., 2021, ApJ, 919, 92

Casella P., Belloni T., Stella L., 2005, ApJ, 629, 403

Chauhan J., et al., 2021, Publ. Astron. Soc. Australia, 38, e045

Corbel S., Fender R. P., Tomsick J. A., Tzioumis A. K., Tingay S., 2004, ApJ, 617, 1272

Del Santo M., Malzac J., Jourdain E., Belloni T., Ubertini P., 2008, MNRAS, 390, 227

Done C., Gierliński M., Kubota A., 2007, A&ARv, 15, 1

Fabian A. C., Rees M. J., Stella L., White N. E., 1989, MNRAS, 238, 729

Fender R. P., 2001, MNRAS, 322, 31

Fender R., 2006, Jets from X-ray binaries. pp 381–419

Fender R. P., Belloni T. M., Gallo E., 2004, MNRAS, 355, 1105

Galeev A. A., Rosner R., Vaiana G. S., 1979, ApJ, 229, 318

García J., et al., 2014, ApJ, 782, 76

García J. A., et al., 2018, ApJ, 864, 25

García F., Méndez M., Karpouzas K., Belloni T., Zhang L., Altamirano D., 2021, MNRAS, 501, 3173

Gilfanov M., 2010, X-Ray Emission from Black-Hole Binaries. p. 17, doi:10.1007/978-3-540-76937-8_2

Haardt F., Maraschi L., 1991, ApJ, 380, L51

Homan J., Wijnands R., van der Klis M., Belloni T., van Paradijs J., Klein-Wolt M., Fender R., Méndez M., 2001, ApJS, 132, 377

Huang Y., et al., 2018, ApJ, 866, 122

Ingram A. R., Motta S. E., 2019, New Astron. Rev., 85, 101524

Ingram A., Done C., Fragile P. C., 2009, MNRAS, 397, L101

Ingram A., Mastroserio G., Dauser T., Hovenkamp P., van der Klis M., García

J. A., 2019, MNRAS, 488, 324

Jiang J., Fürst F., Walton D. J., Parker M. L., Fabian A. C., 2020, MNRAS, 492, 1947

Joinet A., Kalemci E., Senziani F., 2008, ApJ, 679, 655

Kara E., et al., 2019, Nature, 565, 198

Karpouzas K., Méndez M., Ribeiro E. M., Altamirano D., Blaes O., García F., 2020, MNRAS, 492, 1399

Karpouzas K., Méndez M., García F., Zhang L., Altamirano D., Belloni T., Zhang Y., 2021, MNRAS, 503, 5522

Kennea J. A., Evans P. A., Beardmore A. P., Krimm H. A., Romano P., Yamaoka K., Serino M., Negoro H., 2017, The Astronomer's Telegram, 10700, 1

Kong L. D., et al., 2020, Journal of High Energy Astrophysics, 25, 29

Kumar N., Misra R., 2014, MNRAS, 445, 2818

Lee H. C., Miller G. S., 1998, MNRAS, 299, 479

Lee H. C., Misra R., Taam R. E., 2001, ApJ, 549, L229

Ma X., et al., 2021, Nature Astronomy, 5, 94

Maccarone T. J., Coppi P. S., 2003, MNRAS, 338, 189

Méndez M., van der Klis M., 1997, ApJ, 479, 926

Méndez M., Altamirano D., Belloni T., Sanna A., 2013, MNRAS, 435, 2132

Méndez M., Karpouzas K., García F., Zhang L., Zhang Y., Belloni T., Altamirano D., 2022, Nature Astronomy, in press

Merloni A., Fabian A. C., 2001, MNRAS, 321, 549

Miller-Jones J. C. A., et al., 2012, MNRAS, 421, 468

Miller J. M., et al., 2018, ApJ, 860, L28

Mirabel I. F., Rodríguez L. F., 1994, Nature, 371, 46

Mitsuda K., et al., 1984, PASJ, 36, 741

Miyamoto S., Kitamoto S., Mitsuda K., Dotani T., 1988, Nature, 336, 450

Morgan E. H., Remillard R. A., Greiner J., 1997, ApJ, 482, 993

Motta S., Belloni T., Homan J., 2009, MNRAS, 400, 1603

Muñoz-Darias T., Motta S., Belloni T. M., 2011, MNRAS, 410, 679

Negoro H., et al., 2017, The Astronomer's Telegram, 10708, 1

Nowak M. A., 2000, MNRAS, 318, 361

Nowak M. A., Vaughan B. A., Wilms J., Dove J. B., Begelman M. C., 1999, ApJ, 510, 874

Poutanen J., Veledina A., Zdziarski A. A., 2018, A&A, 614, A79

Rawat D., et al., 2022, submitted to MNRAS

Reig P., Belloni T., van der Klis M., Méndez M., Kylafis N. D., Ford E. C., 2000, ApJ, 541, 883

Remillard R. A., McClintock J. E., 2006, ARA&A, 44, 49

Remillard R. A., Morgan E. H., McClintock J. E., Bailyn C. D., Orosz J. A., 1999, ApJ, 522, 397

Russell D. M., Miller-Jones J. C. A., Maccarone T. J., Yang Y. J., Fender R. P., Lewis F., 2011, ApJ, 739, L19

Russell T. D., Miller-Jones J. C. A., Sivakoff G. R., Tetarenko A. J., Jacpot Xrb Collaboration 2017, The Astronomer's Telegram, 10711, 1

Russell T. D., et al., 2019, ApJ, 883, 198

Russell T. D., et al., 2020, MNRAS, 498, 5772

Sridhar N., Bhattacharyya S., Chandra S., Antia H. M., 2019, MNRAS, 487, 4221

Stella L., Vietri M., 1998, ApJ, 492, L59

Stiele H., Kong A. K. H., 2018, ApJ, 868, 71

Stirling A. M., Spencer R. E., de la Force C. J., Garrett M. A., Fender R. P., Ogley R. N., 2001, MNRAS, 327, 1273

Svoboda J., Dovčiak M., Goosmann R. W., Jethwa P., Karas V., Miniutti G., Guainazzi M., 2012, A&A, 545, A106

Tagger M., Pellat R., 1999, A&A, 349, 1003

Tao L., et al., 2018, MNRAS, 480, 4443

Tingay S. J., et al., 1995, Nature, 374, 141

Van der Klis M., 1989, in Ögelman H., van den Heuvel E. P. J., eds, NATO Advanced Study Institute (ASI) Series C Vol. 262, Timing Neutron Stars. p. 27

Vaughan B. A., Nowak M. A., 1997, ApJ, 474, L43

Verner D. A., Ferland G. J., Korista K. T., Yakovlev D. G., 1996, ApJ, 465, 487

Wang J., et al., 2021, ApJ, 910, L3

Wilkins D. R., Fabian A. C., 2012, MNRAS, 424, 1284

Wilms J., Allen A., McCray R., 2000, ApJ, 542, 914

Xu Y., et al., 2018, ApJ, 852, L34

You B., Bursa M., Życki P. T., 2018, ApJ, 858, 82

You B., et al., 2021, Nature Communications, 12, 1025

Zdziarski A. A., Johnson W. N., Magdziarz P., 1996, MNRAS, 283, 193

Zhang S., Lu F. J., Zhang S. N., Li T. P., 2014, in Takahashi T., den Herder J.-W. A., Bautz M., eds, Society of Photo-Optical Instrumentation Engineers (SPIE) Conference Series Vol. 9144, Space Telescopes and Instrumentation 2014: Ultraviolet to Gamma Ray. p. 914421, doi:10.1117/12.2054144

Zhang L., et al., 2020a, MNRAS, 494, 1375

Zhang L., et al., 2020b, MNRAS, 499, 851

Życki P. T., Done C., Smith D. A., 1999, MNRAS, 309, 561

This paper has been typeset from a TEX/LATEX file prepared by the author.